

C. Böckmann | L. Osterloh

Runge-Kutta type regularization method for inversion of spheroidal particle distribution from limited optical data

Suggested citation referring to the original publication:
Inverse Problems in Science and Engineering 22 (2014) 1, 150-165
DOI <https://doi.org/10.1080/17415977.2013.830615>
ISSN (print) 1741-5977
ISSN (online) 1741-5985

Postprint archived at the Institutional Repository of the Potsdam University in:
Postprints der Universität Potsdam
Mathematisch-Naturwissenschaftliche Reihe ; 907
ISSN 1866-8372
<https://nbn-resolving.org/urn:nbn:de:kobv:517-opus4-441200>
DOI <https://doi.org/10.25932/publishup-44120>

Runge-Kutta type regularization method for inversion of spheroidal particle distribution from limited optical data

C. Böckmann* and L. Osterloh

Institut für Mathematik, Universität Potsdam, Potsdam, Germany

(Received 29 July 2013; accepted 29 July 2013)

The Runge-Kutta type regularization method was recently proposed as a potent tool for the iterative solution of nonlinear ill-posed problems. In this paper we analyze the applicability of this regularization method for solving inverse problems arising in atmospheric remote sensing, particularly for the retrieval of spheroidal particle distribution. Our numerical simulations reveal that the Runge-Kutta type regularization method is able to retrieve two-dimensional particle distributions using optical backscatter and extinction coefficient profiles, as well as depolarization information.

Keywords: inverse ill-posed problem; iterative regularization; integral equation; laser remote sensing; inverse scattering; aerosol size distribution

AMS Subject Classifications: 65R32; 47A52; 65R20; 78A46

1. Introduction

Nonlinear ill-posed inverse problems are frequently found in various fields of the natural sciences, ranging, e.g. from sonar sensing of sediments in Geology to measurements of infrared and ultraviolet atmospheric radiation in Atmospheric Physics. They occur wherever a set of measurement data is used to draw conclusions about a set of variables related to the former via a forward model. A straight-forward solution to ill-posed problems is problematic, and regularization methods must be used in order to obtain a solution with physical meaning.

In [1–4], an iterative regularization method known as the Runge–Kutta type regularization method was introduced. The efficiency of this method for aerosol remote sensing was successfully investigated in a series of papers.[5–8] Essentially, optical extinction and backscatter profiles [8] as well as microphysical properties [5–7] of spherical aerosol particles in the atmosphere were inverted from LIDAR-signals (LIght Detection And Ranging) using advanced laser remote sensing techniques.

The goal of this paper is to analyze the applicability of the Runge–Kutta type regularization method for the retrieval of two-dimensional spheroidal particle distribution. The organization of the paper is as follows: In Section 2 we outline the fundamentals of the Runge–Kutta type regularization method by focussing our presentation on the derivation of iteration schemes in continuous and discrete settings. Section 3, explains practical

*Corresponding author. Email: Christine.Boeckmann@uni-potsdam.de

implementation issues concerning the database used, the degree of ill-posedness and the ill-conditionedness of the discretized system. Finally, simulation examples are given.

2. Mathematical formulation

2.1. Runge–Kutta type regularization method in a continuous setting

In atmospheric remote sensing the relationship between the state parameters x encapsulating the two-dimensional spheroidal particle distribution and the set of data y encapsulating the optical coefficient profiles is described by a forward model F . Formally, the retrieval problem is modeled by a Frechet-differentiable nonlinear operator equation

$$F(x) = y, \quad (1)$$

where the forward model operator $F : \mathcal{D}(F) \subset X \rightarrow Y$, acting between the infinite-dimensional real Hilbert spaces X and Y , has a non-closed range of values $\mathcal{R}(F)$, and possesses a locally, uniformly bounded Frechet derivative F' in $\mathcal{D}(F)$. In practice, we can envisage the data $y^\delta \notin \mathcal{R}(F)$ as consisting of noiseless observations $y \in \mathcal{R}(F)$ from a perfect instrument plus a noise component δ , i.e. $y^\delta = y + \delta$. For retrieval problems arising in atmospheric remote sensing, the inverse operator F^{-1} is not continuous, and the solution x^δ of (1), if it exists, with the right-hand side y^δ , does not depend continuously on the data. As a result, the solution is unstable under data perturbation (small errors in the data space Y are dramatically amplified in the state space X) and the problem (1) is said to be ill-posed. It should be remarked that the prototype of ill-posed problems is a Fredholm integral equation of the first kind, and as will be shown in Section 3, our atmospheric retrieval problem requires the solution to this kind of equations. Ill-posed problems can be solved by regularization methods, whereby the solution is stabilized by taking additional information into account.

In this paper, we are concerned with a regularization approach which applies the family of Runge–Kutta methods to the asymptotical regularization method. Initial work on this for the case of linear problems was first done by Böckmann [9], Rieder [4], extended to Padé iteration by Kirsche and Böckmann [3], and later successfully used in active LIDAR remote sensing of the atmosphere to retrieve microphysical aerosol properties.[5] Recently, in [1,2] this method was extended to nonlinear problems. The method of asymptotical regularization can be regarded as a continuous analogue of the Landweber iteration, see [10,11], generated by the particular Runge–Kutta method, namely the explicit Euler method,

$$x_{k+1}^\delta = x_k^\delta + F'(x_k^\delta)^* [y^\delta - F(x_k^\delta)], \quad k = 0, 1, \dots, \quad (2)$$

in which, as shown in [12], a regularized approximation $x^\delta(t)$ of the solution is obtained by solving the initial value problem (Showalter differential equation)

$$\dot{x}^\delta(t) = F'(x^\delta(t))^* [y^\delta - F(x^\delta(t))], \quad 0 < t \leq t_1, \quad x^\delta(0) = x_a. \quad (3)$$

Here, x_a is the a priori state (the best estimate of the solution before solving), $F'(\cdot)^*$ stands for the adjoint operator of $F'(\cdot)$, and the time interval t_1 plays the role of the regularization parameter. The family of Runge–Kutta methods applied to a problem of the form

$$\dot{x}(t) = \Psi(t, x(t)), \quad x(0) = x_a, \quad (4)$$

Table 1. (a)–(c) Butcher tableaux for three second-stage Runge-Kutta methods: Runge, Radau and Lobatto; (d) General Butcher tableau.

$\begin{array}{c cc} 0 & 0 & 0 \\ \hline 1/2 & 1/2 & 0 \\ \hline & 0 & 1 \end{array}$	$\begin{array}{c cc} 1/3 & 5/12 & -1/12 \\ \hline 1 & 3/4 & 1/4 \\ \hline & 3/4 & 1/4 \end{array}$	$\begin{array}{c cc} 0 & 1/2 & -1/2 \\ \hline 1 & 1/2 & 1/2 \\ \hline & 1/2 & 1/2 \end{array}$	$\begin{array}{c c} \mathbf{c} & \mathbf{A} \\ \hline & \mathbf{b}^T \end{array}$
(a) Runge method	(b) Radau method	(c) Lobatto method	(d) General tableau

is characterized by the iterative procedure

$$x_{k+1} = x_k + \tau_k \sum_{i=1}^s b_i \Psi(t + c_i \tau_k, v_i) \quad (5)$$

and

$$v_i = x_k + \tau_k \sum_{j=1}^s a_{ij} \Psi(t + c_j \tau_k, v_j), \quad (6)$$

where τ_k is the step size or the relaxation parameter at the actual iteration step, and $\mathbf{A} = [a_{ij}] \in \mathbb{R}^{s \times s}$, $\mathbf{b} = [b_1, \dots, b_s]^T \in \mathbb{R}^s$, and $\mathbf{c} = [c_1, \dots, c_s]^T \in \mathbb{R}^s$ specify the particular method from the Runge–Kutta family. In particular, s denotes the stage of the Runge-Kutta method. These parameters are often aligned in a Butcher-tableau as shown in Table 1(d).

Applied to the initial value problem (3), following [1], this iterative procedure yields

$$x_{k+1}^\delta = x_k^\delta + \tau_k \sum_{i=1}^s b_i F'(v_i)^* [y^\delta - F(v_i)] \quad (7)$$

and

$$v_i = x_k^\delta + \tau_k \sum_{j=1}^s a_{ij} F'(v_j)^* [y^\delta - F(v_j)]. \quad (8)$$

Setting $z_i = v_i - x_k^\delta$, using the linearization

$$F(v_i) = F(x_k^\delta + z_i) \approx F(x_k^\delta) + F'(x_k^\delta) z_i, \quad (9)$$

and the approximation $F'(v_i) \approx F'(x_k^\delta)$, we express (7) and (8) as

$$x_{k+1}^\delta = x_k^\delta + \tau_k \sum_{i=1}^s b_i F'(x_k^\delta)^* [r_k^\delta - F'(x_k^\delta) z_i] \quad (10)$$

and

$$z_i = \tau_k \sum_{j=1}^s a_{ij} F'(x_k^\delta)^* [r_k^\delta - F'(x_k^\delta) z_j] \quad (11)$$

respectively. In (10) and (11), $r_k^\delta = y^\delta - F(x_k^\delta)$ is the nonlinear residual at the iteration step k . Manipulating (10) and (11) in an appropriate way (see Section 2.2), we end up with the iteration formula

$$x_{k+1}^\delta = x_k^\delta + \tau_k \mathbf{b}^T \Pi_k^{-1} \mathbf{e} F'(x_k^\delta)^* r_k^\delta, \quad (12)$$

where $\mathbf{e} = [1, \dots, 1]^T \in \mathbb{R}^s$,

$$\Pi_k = \mathbf{I}_s + \tau_k \mathbf{A} F'(x_k^\delta)^* F'(x_k^\delta), \tag{13}$$

and $\mathbf{I}_s \in \mathbb{R}^{s \times s}$ is the identity matrix. In [1,2] it was shown that the iteration (12) together with the discrepancy principle as a stopping rule is a convergent regularization method of optimal order under Hölder source conditions, in the sense that the regularized solution converges to the exact solution as the time interval t_1 approaches infinity.

2.2. Runge–Kutta type regularization method in a discrete setting

Applications require a discretization of the state parameter function. Moreover, as any measurement system can deliver only a discrete, finite set of data, the atmospheric retrieval problems we are dealing with are discrete. Essentially, we are faced with the solution of the nonlinear equation

$$\mathbf{F}(\mathbf{x}) = \mathbf{y}, \tag{14}$$

where $\mathbf{x} \in \mathbb{R}^n$ is the vector of state parameters, $\mathbf{y} \in \mathbb{R}^m$ is the data vector, and the vector-valued function $\mathbf{F} : \mathbb{R}^n \rightarrow \mathbb{R}^m$ is the (discrete) forward model. The data vector is supposed to be contaminated by measurement errors, and we write $\mathbf{y}^\delta = \mathbf{y} + \delta$. Because the continuous problem is ill-posed, the underlying discrete problem generally inherits an analogous property and we may say that we are dealing with a discrete ill-conditioned problem. As in a continuous setting, a reliable approximation of the solution can only be obtained by employing a regularization method. The goal of this section is to give a detailed description of the Runge–Kutta type regularization method for solving (14).

Setting $\mathbf{z}_i = [z_{i1}, \dots, z_{in}]^T \in \mathbb{R}^n$ for all $i = 1, \dots, s$, $\mathbf{K}_k = \mathbf{F}'(\mathbf{x}_k^\delta) \in \mathbb{R}^{m \times n}$ and $\mathbf{r}_k^\delta = \mathbf{y}^\delta - \mathbf{F}(\mathbf{x}_k^\delta)$, the discrete versions of (10) and (11) become

$$\mathbf{x}_{k+1}^\delta = \mathbf{x}_k^\delta + \tau_k \sum_{i=1}^s b_i \mathbf{K}_k^T (\mathbf{r}_k^\delta - \mathbf{K}_k \mathbf{z}_i), \tag{15}$$

and

$$\mathbf{z}_i = \tau_k \sum_{j=1}^s a_{ij} \mathbf{K}_k^T (\mathbf{r}_k^\delta - \mathbf{K}_k \mathbf{z}_j), \tag{16}$$

respectively. Putting $\mathbf{Z} = [\mathbf{z}_1, \dots, \mathbf{z}_s]^T \in \mathbb{R}^{s \cdot n}$, we express (16) in matrix form as

$$(\mathbf{I}_s \otimes \mathbf{I}_n) \mathbf{Z} = \tau_k (\mathbf{A} \otimes \mathbf{I}_n) \begin{bmatrix} \mathbf{K}_k^T \mathbf{r}_k^\delta \\ \vdots \\ \mathbf{K}_k^T \mathbf{r}_k^\delta \end{bmatrix} - \tau_k (\mathbf{A} \otimes \mathbf{K}_k^T \mathbf{K}_k) \mathbf{Z}, \tag{17}$$

where the notation $\mathbf{A} \otimes \mathbf{B}$ stands for the Kronecker product of the matrices $\mathbf{A} \in \mathbb{R}^{m \times n}$ and $\mathbf{B} \in \mathbb{R}^{k \times p}$, i.e.

$$\mathbf{A} \otimes \mathbf{B} = \begin{pmatrix} a_{11} \mathbf{B} & a_{12} \mathbf{B} & \dots & a_{1n} \mathbf{B} \\ a_{21} \mathbf{B} & a_{22} \mathbf{B} & \dots & a_{2n} \mathbf{B} \\ \vdots & \vdots & & \vdots \\ a_{m1} \mathbf{B} & a_{m2} \mathbf{B} & \dots & a_{mn} \mathbf{B} \end{pmatrix}_{(m \cdot k) \times (n \cdot p)}.$$

The use of the Kronecker product enables us to derive a transparent solution representation in a straightforward manner. Some calculation rules involving the Kronecker product are given in Appendix A. From (17) we get

$$\left[\mathbf{I}_{sn} + \tau_k (\mathbf{A} \otimes \mathbf{K}_k^T \mathbf{K}_k) \right] \mathbf{Z} = \tau_k (\mathbf{A} \otimes \mathbf{I}_n) \left(\mathbf{e} \otimes \mathbf{K}_k^T \mathbf{r}_k^\delta \right). \quad (18)$$

where $\mathbf{I}_{sn} = \mathbf{I}_s \otimes \mathbf{I}_n$. Hence, assuming that

$$\Pi_k = \mathbf{I}_{sn} + \tau_k (\mathbf{A} \otimes \mathbf{K}_k^T \mathbf{K}_k), \quad (19)$$

some properties of which are discussed in more detail in Appendix B, is regular, gives us

$$\mathbf{Z} = \tau_k \Pi_k^{-1} (\mathbf{A} \otimes \mathbf{I}_n) (\mathbf{e} \otimes \mathbf{K}_k^T \mathbf{r}_k^\delta). \quad (20)$$

Going back to (15) and using (B1) of Appendix B,

$$\Pi_k^{-1} = \mathbf{I}_{sn} - \left(\mathbf{I}_s \otimes \mathbf{K}_k^T \mathbf{K}_k \right) \tau_k \Pi_k^{-1} (\mathbf{A} \otimes \mathbf{I}_n),$$

an implicit representation of the inverse, yields

$$\begin{aligned} \mathbf{x}_{k+1}^\delta &= \mathbf{x}_k^\delta + \tau_k \left(\mathbf{b}^T \otimes \mathbf{I}_n \right) \left(\mathbf{e} \otimes \mathbf{K}_k^T \mathbf{r}_k^\delta \right) - \tau_k \left(\mathbf{b}^T \otimes \mathbf{I}_n \right) \left(\mathbf{I}_s \otimes \mathbf{K}_k^T \mathbf{K}_k \right) \mathbf{Z} \\ &= \mathbf{x}_k^\delta + \tau_k \left(\mathbf{b}^T \otimes \mathbf{I}_n \right) \left[\mathbf{I}_{sn} - \left(\mathbf{I}_s \otimes \mathbf{K}_k^T \mathbf{K}_k \right) \tau_k \Pi_k^{-1} (\mathbf{A} \otimes \mathbf{I}_n) \right] \left(\mathbf{e} \otimes \mathbf{K}_k^T \mathbf{r}_k^\delta \right) \\ &= \mathbf{x}_k^\delta + \tau_k \left(\mathbf{b}^T \otimes \mathbf{I}_n \right) \Pi_k^{-1} \left(\mathbf{e} \otimes \mathbf{K}_k^T \mathbf{r}_k^\delta \right). \end{aligned} \quad (21)$$

In the particular case $s = 2$ considered here, (21) reduces to

$$\mathbf{x}_{k+1}^\delta = \mathbf{x}_k^\delta + \begin{bmatrix} b_1 \mathbf{I}_n & b_2 \mathbf{I}_n \end{bmatrix} \left(\alpha_k \mathbf{I}_{2n} + \begin{bmatrix} a_{11} \mathbf{K}_k^T \mathbf{K}_k & a_{12} \mathbf{K}_k^T \mathbf{K}_k \\ a_{21} \mathbf{K}_k^T \mathbf{K}_k & a_{22} \mathbf{K}_k^T \mathbf{K}_k \end{bmatrix} \right)^{-1} \begin{bmatrix} \mathbf{K}_k^T \mathbf{r}_k^\delta \\ \mathbf{K}_k^T \mathbf{r}_k^\delta \end{bmatrix} \quad (22)$$

where we used the notation $\alpha_k = 1/\tau_k$. Some of the most popular Runge–Kutta type methods of the second stage include the Runge method, the Radau method and the Lobatto method, whose Butcher tableaus are illustrated in Table 1(a)–(c). The Runge method, notably, is ill suited for our purposes, since it is not A-stable, see Appendix C. The Radau and Lobatto methods, however, are perfectly suitable—both of them are A-stable. Fortunately, this means that the step size τ_k can theoretically be chosen arbitrarily large, and this choice reduces the number of iteration steps drastically in contrast to (2).

It should be pointed out that for the explicit Euler iteration ($s = 1$, $a_{11} = 0$, $b_1 = 1$) we are left with $\mathbf{z}_1 = \mathbf{0}$, and (15) is the nonlinear Landweber iteration. For the implicit Euler method ($s = 1$, $a_{11} = 1$, $b_1 = 1$), (21) reads as

$$\mathbf{x}_{k+1}^\delta = \mathbf{x}_k^\delta + (\alpha_k \mathbf{I}_n + \mathbf{K}_k^T \mathbf{K}_k)^{-1} \mathbf{K}_k^T \mathbf{r}_k^\delta, \quad (23)$$

and coincides with the iteration formula of the regularizing Levenberg–Marquardt method, see [11,13–15]. This equivalence shows the role of the inverse of the step size α_k : It takes on the role of a second parameter which controls the amount of constraint at each iteration step. The parameters α_k are usually chosen as the terms of a decreasing sequence. This is because at the beginning of the iterative process large α_k values avoid local minima and ensure that the (linearized) problem is better conditioned, while at the end of the iterative process small α_k values lower the importance of the constraint and yield a stable solution.

However, it should not be too small, i.e. the step size τ_k should not be too large, since otherwise the discrepancy principle could be overshoot with the last iteration step.

In the next Section, we apply the Radau method, see Table 1(b), to an atmospheric problem from remote sensing.

3. Application

Studying the influence of non-spherical cloud and aerosol particles on the radiation budget of Earth's atmosphere is of growing importance in remote sensing. Saharan dust storms as well as volcanic eruptions are, e.g. sources of non-spherical aerosol particles which are important for a better understanding of the direct and indirect climate effects of such global events. We conduct our investigation with the inversion of the size distribution function from limited LIDAR data.

We consider here an ensemble of spheroidal particles characterized by the complex refractive index m and the aspect ratio a , while r is the radius of a volume-equivalent sphere.

A spheroid is created by rotating the curve C defined by

$$C(\vartheta) = r_h \left(\sin^2 \vartheta + a^2 \cos^2(\vartheta) \right)^{-1/2}, \quad \vartheta \in [0, \pi], \quad (24)$$

see Figure 1 for examples of oblate and prolate spheroids.

Let us denote by r_h the horizontal semi-axis of the spheroid, and by r_v the vertical one. This means the aspect ratio $a = r_v/r_h$. The problem consists in retrieving the volume size distribution function $v(r, a)$ of the spheroidal particle ensemble from the optical particle properties. The inversion will be performed with the following optical data Γ_j : the direct-polarization particle backscatter coefficient β at 355, 532 and 1064 nm and the cross-polarization component of the particle backscatter coefficient δ at 355, 532 and 1064 nm as well as the particle extinction coefficient α at 355 and 532 nm (in sum: $3\beta + 3\delta + 2\alpha$ wavelengths λ). Since we will assume r denotes the radius of the volume-equivalent sphere, the volume distribution is $v(r, a) = \frac{4\pi r^3}{3} n(r, a)$, where $n(r, a)$ is the number size distribution. The volume distribution is used since it is less prone to numerical instabilities than the size distribution $n(r, a)$, see [16]. We can model the inverse ill-posed retrieval problem with the spheroidal efficiencies Q_j , $j \in \{\beta, \delta, \alpha\}$ from the scattering database for spheroidal particles,[17] see Table 2, and the spheroid surface S as

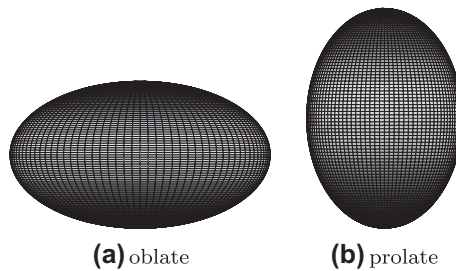


Figure 1. Two spheroids. On the left, an oblate spheroid with aspect ratio $a = 0.5$, on the right, a prolate spheroid with $a = 1.5$.

Table 2. Refractive indices m and aspect ratios a of the database.

$\Re(m)$	1.33	1.4	1.5	1.6	1.7	1.8	
$\Im(m)$	0	0.001	0.005	0.01	0.03	0.05	0.1
a	0.67	0.77	0.87	1.0	1.15	1.3	1.5

$$\Gamma_j(\lambda) = \int_{a_{\min}}^{a_{\max}} \int_{r_{\min}}^{r_{\max}} \frac{3S}{16\pi r^3} Q_j(r, \lambda, m, a) v(r, a) dr da. \quad (25)$$

Thus, the integral over the radius is integrated again over a parameter representing the different aspect ratios. Here the direct problem consists in calculating $\Gamma_j(\lambda)$ from a given distribution $v(r, a)$ whereas the inverse problem means the determination of $v(r, a)$ from given data $\Gamma_j(\lambda)$. More precisely, this means here that we are looking for two-dimensional distributions from given optical data; for more details see [16]. The retrieval problem of the distribution from the above two-dimensional Fredholm system of the first kind, i.e. the underlying operator is compact, is ill-posed in nature, and therefore requires particular regularization techniques. In case the complex refractive index is fixed and known a-posteriori the model (25) is a linear one. Iterative regularization methods are very appropriate to solve Equation (25) for $v(r, a)$. The well-known Landweber iteration is very slow, therefore, even for linear problems the iteration methods with A-stable Butcher tableaux from Section 2 are very advantageous here.

3.1. Degree of Ill-posedness and simulations

An interesting question when considering spheroids with a fixed aspect ratio is to what extent this affects the ill-posedness of the problem. It is known that the singular values of a compact operator approach zero, i.e. $\lim_{j \rightarrow \infty} \sigma_j = 0$. The faster the decay rate, the more “ill-posed” the operator problem becomes, and the more difficult the solution process is. A problem is said to be ill-posed of degree $\mu \in \mathbb{R}^+$ if we have $\sigma_j \sim j^{-\mu}$ for $j \rightarrow \infty$. In other words, it is helpful in such worst cases to include additional a-priori information into the solution process. Here we will also use cross-polarization particle backscatter coefficient profiles.

Intuitively, we would assume that the degree of ill-posedness is slightly dependent on the aspect ratio, and grows along with increasing non-sphericity. Therefore, in Figure 2 we have plotted the degree of ill-posedness of the corresponding one-dimensional operator of Equation (25) for extinction and backscatter dependent on the fixed aspect ratio a for two different refractive indices, non-absorbing $m = 1.5$ and absorbing $m = 1.5 + 0.01i$. We have numerically calculated an approximation of the degree of ill-posedness for 20 different fixed values between $a = 0.67$ and $a = 1.5$; for more details see [16,18]. As one can see in Figure 2, the effect that we have predicted from observing efficiency functions is obviously present here. The larger the non-sphericity of the particles, the higher the degree of ill-posedness. It is interesting to see that the additional effect of the refractive index seems to be, more or less, additive in nature; the curves for the two different indices look more or less the same, the degree for the absorbing refractive index is about 1 or 1.5 higher for extinction or backscatter, respectively. The difference in the degree for spherical and highly a-spherical particles is much more pronounced for backscatter than for extinction. However, in sum, the increase in ill-posedness is not very significant and the degree is still moderate for spheroidal particles as it is for spheres.

In the inversion process of the corresponding one-dimensional system of Equation (25) the aspect ratio has a large influence as the following simulation shows. The inversion will be performed with error-free simulated data, $3\beta + 3\delta + 2\alpha$ wavelengths (direct-polarization and cross-polarization backscatter at 355, 532 and 1064 nm and extinction at 355 and 532 nm) for the complex refractive index $m = 1.5 + 0.01i$. In Figure 3(a), the forward calculation with a distribution as described in Equation (28), a fixed aspect ratio of $a = 1.15$ and a refractive index of $m = 1.5 + 0.01i$ was done, and afterwards inverted with the exact refractive index but with different aspect ratios. As one can see, the reconstruction works very well for the correct aspect ratio of $a = 1.15$. On the other hand, the reconstruction fails completely for all other assumed aspect ratios; even correctly assuming prolate particles, but with an incorrect aspect ratio of $a = 1.5$, leads to completely worthless results here.

Figure 3(b) is the same example with a true aspect ratio of $a = 0.67$, thus an ensemble of oblate spheroids. Basically the same behavior is exhibited here; the distribution is reconstructed very well for the correct aspect ratio, and it fails completely for any incorrect fixed aspect ratio.

Basically, assuming a wrong aspect ratio for spheroids is very similar to choosing a wrong refractive index for spheres; as the corresponding kernel functions for different aspect ratios or refractive indices wildly fluctuate, reconstruction fails completely when a different kernel function is used for the forwards and backwards models. Therefore, it is useful and even necessary to investigate and use in application scenarios the two-dimensional (2D) model Equation (25).

Another interesting question concerns the condition number of the matrix after discretization of the Fredholm system. In Figure 2(c) and (d) we show the transition from infinite-dimensional to finite-dimensional spaces, which depends very much on the discretization itself; for more details see [19]. After discretization of Equation (25) by collocation, the degree of ill-posedness can be expressed with the condition number $\kappa = \frac{\sigma_{\max}}{\sigma_{\min}}$. This effectively produces the factor by which a given disturbance in the data can be amplified. In Figure 2(c) and (d) we have plotted the logarithms (base 10) of the condition numbers κ of the matrices A^C , see Equation (26), resulting for B-spline collocation discretization of Equation (25), dependent on the complex refractive index. We have assumed realistic values that do not include any a priori information, thus $r_{\min} = 10^{-4} \mu\text{m}$, $r_{\max} = 2 \mu\text{m}$, $\lambda = (355_{\alpha}, 355_{\beta}, 532_{\alpha}, 532_{\beta}, 1064_{\beta} \text{ nm})$ for spheres and $\lambda = (355_{\alpha}, 355_{\beta}, 355_{\delta}, 532_{\alpha}, 532_{\beta}, 532_{\delta}, 1064_{\beta}, 1064_{\delta} \text{ nm})$ for spheroids, respectively, as well as a B-spline basis of order 4 and 9 equidistantly distributed base points. Our limited data points are 5 data points for spheres and 8 data points for spheroids, respectively.

As shown in Figure 2(c), the condition numbers, spherical case $a = 1$, are in the order of magnitude between 1 and 3. In detail, they are growing with an increasing imaginary part $\Im(m)$ and roughly with a decreasing real part $\Re(m)$ of the complex refractive index.

In Figure 2(d) we have plotted the spheroidal condition numbers of the resulting spline collocation matrices. The qualitative behavior is more or less the same as for spheres, particularly the monotonic behavior with an increasing imaginary part. The different behavior of the real part is an ongoing investigation. Furthermore, the orders of magnitude of the condition numbers are slightly higher, ranging from 2 to 4 as one would expect from the ill-posedness shown in Figure 2(a) and (b). Therefore, we have to use an appropriated iterative regularization technique to solve Equation (25) for $v(r, a)$ as mentioned before, e.g. the iterative regularizing Radau method from Section 2.

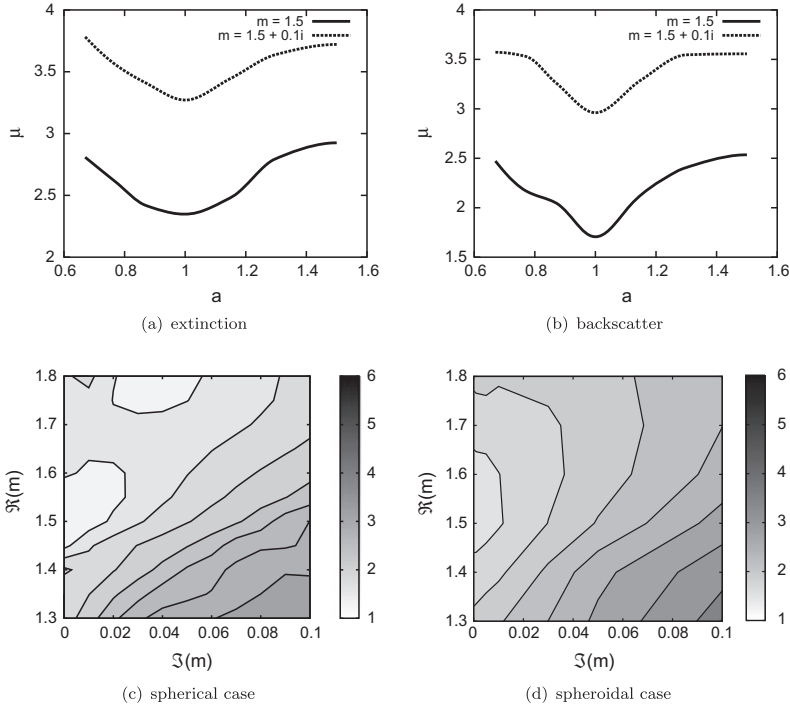


Figure 2. (a) and (b): Degrees of ill-posedness of the infinite dimensional model for two different refractive indices. (c) and (d): The condition numbers κ of the collocation matrices A^C resulting from discretizing the problem. Scale: $\log_{10} \kappa(A^C)$.

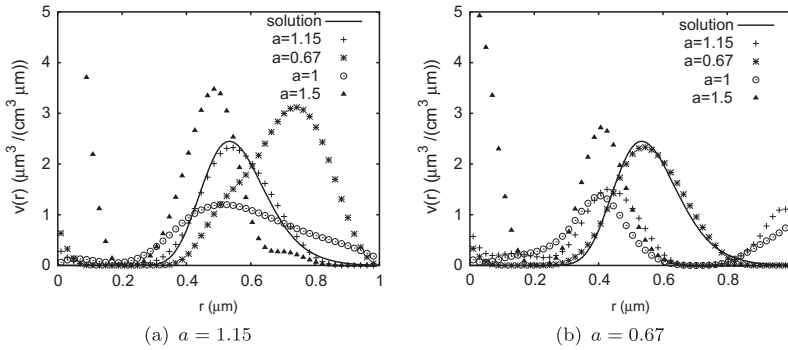


Figure 3. Reconstruction of a particle distribution with fixed aspect ratio $a = 1.15$ and $a = 0.67$, inverted assuming different aspect ratios using a mono-modal log-normal distribution with $r_{\text{med}} = 0.5 \mu\text{m}$, $\sigma = 1.2$ and $N_t = 1 \text{cm}^{-3}$.

The spline collocation matrix is given by

$$A_{i,\tau(l,k)}^C = \int_{a_{\min}}^{a_{\max}} \int_{r_{\min}}^{r_{\max}} \frac{3S}{16\pi r^3} Q_j(r, \lambda_i, m, a) \Phi_{l,k}(r, a) dr da, \quad (26)$$

where $\Phi_{l,k}(r, a)$ ($l = 1, \dots, l_r; k = 1, \dots, l_a; i = 1, \dots, l_\Gamma$) is the two-dimensional B-spline basis, i.e. describes the B-spline surface, meaning that $A^C \in \mathbb{R}^{l_\Gamma, l_r l_a}$. $\tau(l, k)$ is a one-dimensional rearranging for the indices l and k and $\tau^{-1}(j)$ is the inverse, i.e. the back-rearranging. We solve the inverse problem $A^C x = \Gamma$, and obtain our reconstructed volume distribution by

$$v(r, a) = \sum_{j=1}^{l_r l_a} x_j \Phi_{\tau^{-1}(j)}(r, a) \quad (27)$$

using a projected Radau iteration since we have to determine a non-negative distribution, see [20,21]. Moreover, the iteration stops using Morozov's well-known discrepancy principle; for more details see [7].

3.2. Simulation results of the 2D model

To evaluate the validity of the proposed 2D model and algorithm, we first tested it on data simulated from spherical particles. We used simulated data gained from the 1D spherical forward model (direct problem) assuming the mono-modal ($M = 1$) log-normal distribution with $r_{\text{med}} = 0.1 \mu\text{m}$, $\sigma = 1.6$, $N_t = 1 \text{ cm}^{-3}$ with $m = 1.5 + 0.01i$ at extinction wavelengths of 355 and 532 nm and backscatter wavelengths at 355, 532 and 1064 nm, i.e.

$$n(r) = \sum_{j=1}^M \frac{N_{t,j}}{\sqrt{2\pi r \ln \sigma_j}} \exp\left(\frac{(\ln r - \ln r_{\text{med},j})^2}{-2(\ln \sigma_j)^2}\right). \quad (28)$$

The inversion results with the 2D model (inverse problem) are shown in Figure 4. We performed the inversion with noiseless data. Consider first Figure 4(b), 4(d) and 4(f), in which we used the spherical forward data as described above. Not surprisingly, while the aspect-ratio-integrated distribution $v_a(r)$ in Figure 4(d) can be calculated quite exactly, the radius-integrated distribution over the aspect ratios $v_r(a)$ as shown in 4(f) is very far from correct; the true solution is only a delta peak at $a = 1$.

For the other three figures on the left, Figure 4(a), (c) and (e), we have also incorporated depolarization information, i.e. cross-polarization backscatter coefficients. This means that in addition to the data points at $355_\alpha, 355_\beta, 532_\alpha, 532_\beta$ and 1064_β nm we included $355_\delta, 532_\delta$ and 1064_δ nm for the 2D inversion. The three additional values are of course zero, as one knows that spherical particles will not result in any cross-polarization backscatter. As one can see from the figures, while the reconstruction of $v_a(r)$ is nearly identical, the reconstruction of $v_r(a)$ works much better in this case as expected.

This leads to a very interesting proposition, which we will further investigate in other examples; while information about the sizes of the particles are mostly included in the extinction and total backscatter data, the shape of the particles (here represented by the aspect ratio) can only be reliably determined with knowledge of the depolarization.

Secondly, we will move on to real simulation examples which consist of ensembles of spheroids with variable aspect ratios.

For our simulations, we used distributions that assume a uniform mono-modal log-normal distribution with respect to the radius, multiplied by a weighting function $w(a)$ over the different aspect ratios. Note that we basically only define the $w(a)$ on the seven

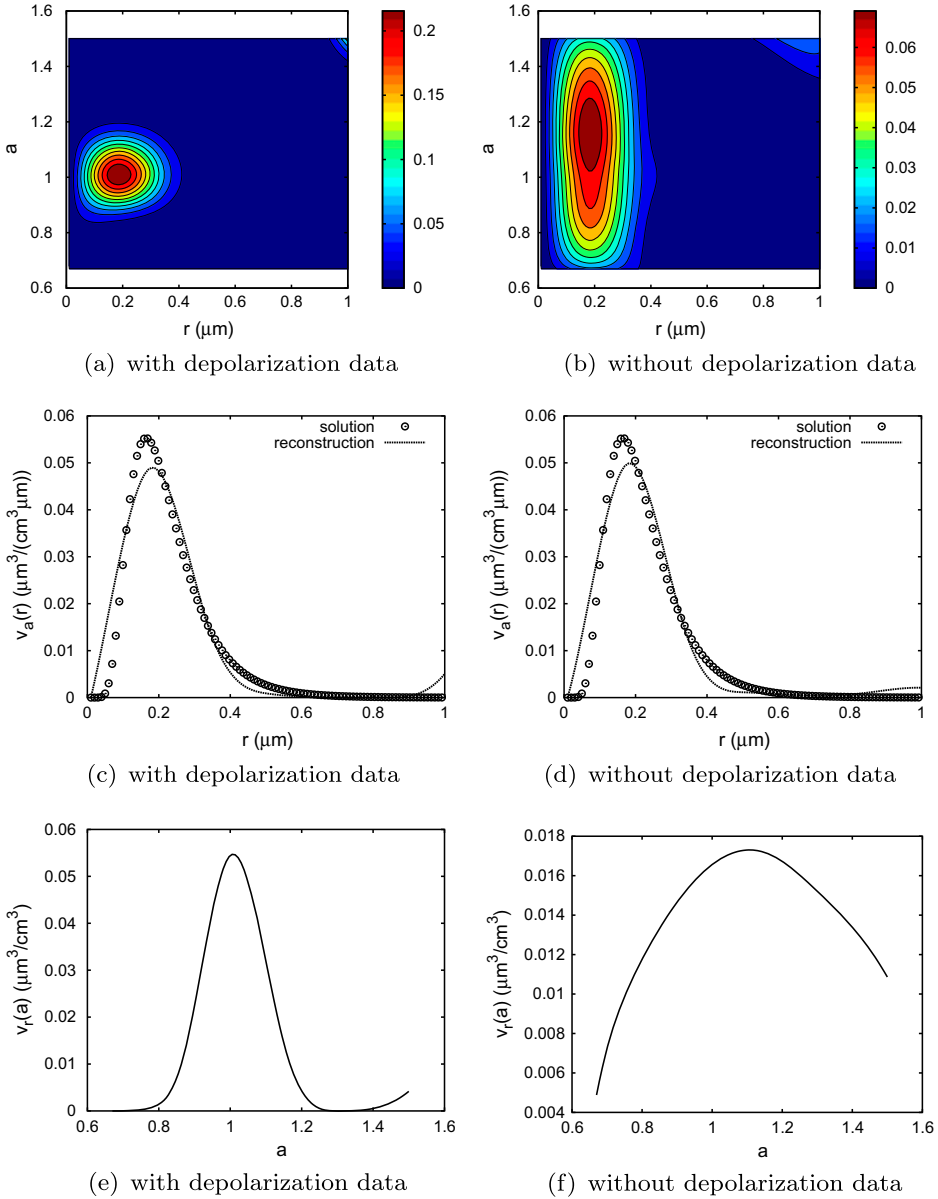


Figure 4. Inverting data gained from a spherical forward model with a mono-modal log-normal distribution and a complex refractive index of $m = 1.5 + 0.01i$. For (e) and (f) the exact solution is a delta peak at $a = 1$.

aspect ratios we have available in the database – everything else must be interpolated. We perform our evaluations with two-dimensional volume distributions calculated by

$$v_j(r, a) = \frac{4\pi r^3}{3} n(r) \cdot w_j(a), \quad (29)$$

Table 3. Test cases for two-dimensional distribution retrieval.

Case	r_{med}	σ	N_t	$w(a)$
1	0.5	1.2	1	$w_1(a) = \begin{cases} 1/3, & a = 1.15, \\ 1/3, & a = 1 \vee a = 1.3 \\ 0 & \text{otherwise} \end{cases}$
2	0.1	1.6	100	$w_2(a) = \begin{cases} 0.5, & a = 0.67 \vee a = 0.77 \\ 0 & \text{otherwise} \end{cases}$
3	0.1	1.6	100	$w_3(a) = \begin{cases} 0.5, & a = 1.3 \vee a = 1.5 \\ 0 & \text{otherwise} \end{cases}$

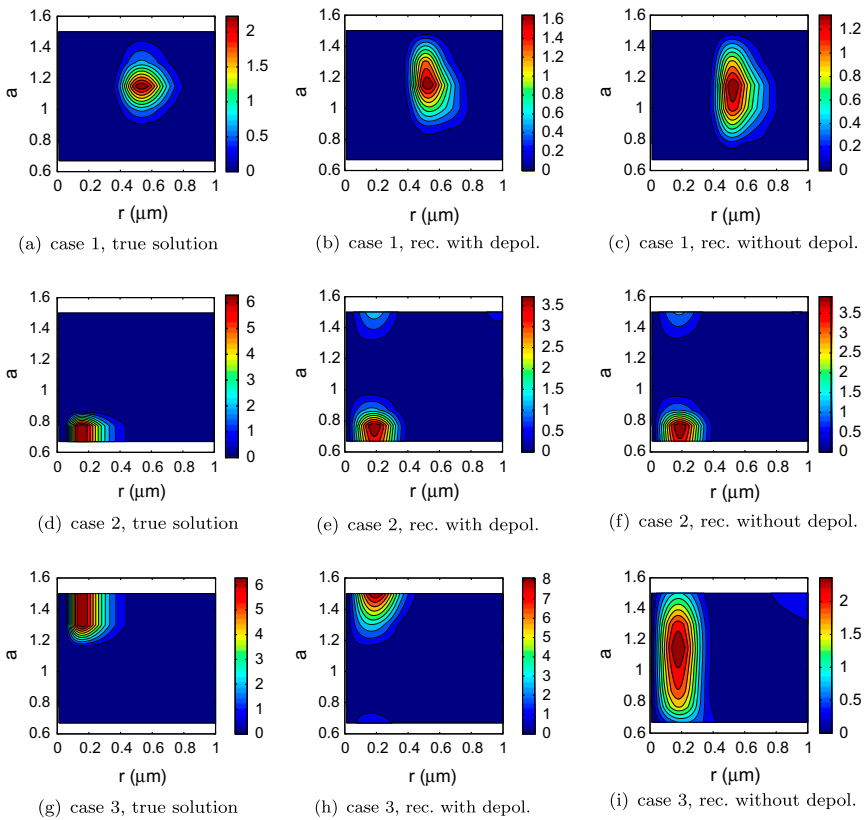


Figure 5. Reconstructions with and without depolarization data for the three cases from Table 3.

where j is the number of the case taken from Table 3. We will assume a refractive index of $m = 1.5 + 0.01i$ for both forward and inversion calculations.

In the examples from Table 3, case 2 represents an ensemble of solely oblate particles, case 3 an ensemble of solely prolate particles while case 1 contains a mixture of prolate particles with spheres.

After simulating the forward calculation with these particle distributions according to Equation (25), we try to invert the optical coefficients gained to reconstruct the volume distribution. We will do this in two different ways, first while ignoring all potential depolarization information, i.e. $l_{\Gamma} = 5$, and second with the assumption that we cleanly separate the direct-polarization and cross-polarization fractions of the total backscatter coefficients, i.e. $l_{\Gamma} = 8$. These two approaches lead to completely different results in some cases. We will see that sometimes, especially for oblate particles, depolarization information does not play a big role in obtaining a good reconstruction of the volume distribution, while it is absolutely necessary for prolate particles with respect to our selected examples.

We look at reconstruction results gained from inverting noiseless data, see Figure 5. Interestingly, the radius-averaged volume distribution is reconstructed with good quality for all cases, whether we consider the depolarization information or not. The situation looks much different for the aspect-ratio-averaged volume distribution results. For case 3, the ensemble of prolate particles, the reconstruction with respect to the aspect ratio fails completely, as shown in Figure 5(i). Whether in general prolate ensembles are much more difficult to reconstruct than oblate ones is a question in need of further investigation. But it leads us to the confirmation that it is the depolarization information that may contain the crucial information about the aspect ratio distribution of the particles.

3.3. Summary and conclusion

In this application Section, a model used for the forward calculation and inversion of aerosol optical properties that is based on Mie theory and used for spheres with limited input data has been extended to work on spheroids, where the underlying kernel functions were exchanged with database values that have been calculated via a T-matrix method, see [17,22]. Furthermore, we have investigated the role that depolarization information plays in this inversion. Experiments have shown that the importance of depolarization information is highly dependent on each individual case. This, of course, implies the high significance of availability of these separated direct-polarization and cross-polarization backscatter coefficient profiles, since results can be completely invalidated in some cases if there is no depolarization information present. This is a very important result for inversion of remote sensing data, as we showed that the availability of good depolarization information is what makes inversion of optical particle profiles of ensembles of spheroidal particles towards microphysical particle properties workable.

The determination of the size distribution function is very important, since from it one can calculate all microphysical properties in a straightforward manner, in particularly the single scattering albedo of aerosol necessary as input for climate models to predict global warming or cooling.

Further interesting and important tasks in future arise in examinations of non-spherical particle shapes with edges.

Acknowledgements

This work was supported partially by the European Union seventh framework program through the ITARS project 289923. It is a great pleasure for the authors to thank Tom Rother and Adrian Doicu for very fruitful discussions.

References

- [1] Böckmann C, Pornsawad P. Iterative Runge-Kutta-type methods for nonlinear ill-posed problems. *Inverse Probl.* 2008;2:025002.
- [2] Pornsawad P, Böckmann C. Convergence rate analysis of the first-stage Runge-Kutta-type regularizations. *Inverse Probl.* 2010;2:035005.
- [3] Kirsche A, Böckmann C. Padé iteration method for regularization. *Appl. Math. Comput.* 2006;180:648–663.
- [4] Rieder A. Runge-Kutta integrators yield optimal regularization schemes. *Inverse Probl.* 2005;21:453–471.
- [5] Böckmann C, Kirsche A. Iterative regularization method for lidar remote sensing. *Comput. Phys. Commun.* 2006;174:607–615.
- [6] Osterloh L, Pérez C, Böhme D, Baldasano JM, Böckmann C, Schneidenbach L, Vicente D. Parallel software for retrieval of aerosol distribution from lidar data in the framework of EARLINET-ASOS. *Comput. Phys. Comm.* 2009;180:2095–2102.
- [7] Osterloh L, Böckmann C, Mamouri R, Papayannis A. An adaptive base point algorithm for the retrieval of aerosol microphysical properties. *The Open Atmos. Sci. J.* 2011;5:61–73.
- [8] Pornsawad P, D’Amico G, Böckmann C, Amodeo A, Pappalardo G. The retrieval of aerosol extinction coefficient profiles from Raman lidar data by inversion. *Appl. Opt.* 2012;51:2035–2044.
- [9] Böckmann C. Runge-Kutta type methods for Ill-posed problems and the retrieval of aerosol size distributions. *PAMM.* 2002;1:486–487.
- [10] Engl H, Hanke M, Neubauer A. *Regularization of inverse problems.* Dordrecht: Kluwer; 2000.
- [11] Kaltenbacher B, Neubauer A, Scherzer O. *Iterative Regularization Methods for Nonlinear Ill-posed Problems.* Berlin: de Gruyter; 2008.
- [12] Tautenhahn U. On the asymptotical regularization of nonlinear ill-posed problems. *Inverse Probl.* 1994;10:1405–1418.
- [13] Vasin V. The Levenberg-Marquardt method for approximation of solutions of irregular operator equations. *Automat. Rem. Contr.* 2012;73:440–449.
- [14] Hanke M. The regularizing Levenberg-Marquardt scheme is of optimal order. *Integral Equations Appl.* 2010;22:259–283.
- [15] Hochbruck M, Höning M. On the convergence of a regularizing Levenberg-Marquardt scheme for nonlinear ill-posed problems. *Numer. Math.* 2010;115:71–79.
- [16] Osterloh L. *Retrieving aerosol microphysical properties from multiwavelength lidar data [Ph.D. Thesis]:* Potsdam University; 2011.
- [17] Schmidt K, Wauer J, Rother T, Trautmann T. Scattering database for spheroidal particles. *Appl. Opt.* 2009;48:2154–2164.
- [18] Hansen P. Computation of the singular value expansion. *Computing.* 1988;40:185–199.
- [19] Osterloh L, Böckmann C, Nicolae D, Nemuc A. Regularized inversion of microphysical atmospheric particle parameters: Theory and application. *J. Comput. Phys.* 2013;237:79–94.
- [20] Eicke B. Iteration methods for convexly constrained ill-posed problems in Hilbert space. *Numer. Funct. Anal. and Optimiz.* 1992;13:413–429.
- [21] Vogel C. *Computational Methods for Inverse Problems.* Philadelphia: SIAM; 2002.
- [22] Mishchenko M, Travis L, Lacis Scattering A. *Absorption, and emission of light by small particles.* New York: NASA Goddard Institute for Space Studies; 2005.
- [23] Schmidt K, Trenkler G. *Einführung in die Moderne Matrix-Algebra.* Berlin: Springer; 2006.

Appendix A. The Kronecker product

We report here the definition and the principal properties of the Kronecker product of matrices, see e.g. [23]. Let $\mathbf{A} = (a_{ij}) \in \mathbb{R}^{m \times n}$ and $\mathbf{B} \in \mathbb{R}^{k \times p}$, in which case the matrix

$$\mathbf{A} \otimes \mathbf{B} := \begin{pmatrix} a_{11}\mathbf{B} & a_{12}\mathbf{B} & \dots & a_{1n}\mathbf{B} \\ a_{21}\mathbf{B} & a_{22}\mathbf{B} & \dots & a_{2n}\mathbf{B} \\ \vdots & \vdots & & \vdots \\ a_{m1}\mathbf{B} & a_{m2}\mathbf{B} & \dots & a_{mn}\mathbf{B} \end{pmatrix}_{(mk) \times (np)} \quad (\text{A1})$$

is called the *Kronecker* (or *tensor*) *product* of \mathbf{A} and \mathbf{B} .

Let \mathbf{A} , \mathbf{B} , \mathbf{C} and \mathbf{D} be matrices such that all the operations below reported are defined. Then:

- (i) for all $\alpha \in \mathbb{R}$: $(\alpha\mathbf{A}) \otimes \mathbf{B} = \mathbf{A} \otimes (\alpha\mathbf{B}) = \alpha(\mathbf{A} \otimes \mathbf{B})$;
- (ii) $(\mathbf{A} + \mathbf{B}) \otimes \mathbf{C} = (\mathbf{A} \otimes \mathbf{C}) + (\mathbf{B} \otimes \mathbf{C})$;
- (iii) $\mathbf{A} \otimes (\mathbf{B} + \mathbf{C}) = (\mathbf{A} \otimes \mathbf{B}) + (\mathbf{A} \otimes \mathbf{C})$;
- (iv) $\mathbf{A} \otimes (\mathbf{B} \otimes \mathbf{C}) = (\mathbf{A} \otimes \mathbf{B}) \otimes \mathbf{C}$;
- (v) $(\mathbf{A} \otimes \mathbf{B})^T = \mathbf{A}^T \otimes \mathbf{B}^T$;
- (vi) $(\mathbf{A} \otimes \mathbf{B})(\mathbf{C} \otimes \mathbf{D}) = (\mathbf{A}\mathbf{C}) \otimes (\mathbf{B}\mathbf{D})$;
- (vii) for all $\mathbf{A} \in \mathbb{R}^{n \times n}$ and $\mathbf{B} \in \mathbb{R}^{m \times m}$:
 $\mathbf{A} \otimes \mathbf{B} = (\mathbf{A} \otimes \mathbf{I}_m)(\mathbf{I}_n \otimes \mathbf{B}) = (\mathbf{I}_n \otimes \mathbf{B})(\mathbf{A} \otimes \mathbf{I}_m)$
- (viii) if \mathbf{A} and \mathbf{B} are nonsingular matrices: $(\mathbf{A} \otimes \mathbf{B})^{-1} = \mathbf{A}^{-1} \otimes \mathbf{B}^{-1}$;
- (ix) for all $\mathbf{A} \in \mathbb{R}^{n \times n}$ and $\mathbf{B} \in \mathbb{R}^{m \times m}$: $\det(\mathbf{A} \otimes \mathbf{B}) = \det(\mathbf{A})^m \det(\mathbf{B})^n$.

Appendix B. Properties of Π

In this appendix, we show that the inverse of Π has the implicit representation

$$\Pi^{-1} = \mathbf{I}_{sn} - \tau(\mathbf{I}_s \otimes \mathbf{K}^T \mathbf{K})\Pi^{-1}(\mathbf{A} \otimes \mathbf{I}_n), \quad (\text{B1})$$

where we cut the iteration index k for brevity's sake. Starting with (19) and using (Appendix A..(vii)), we get

$$\begin{aligned} \Pi &= \mathbf{I}_{sn} + \tau(\mathbf{A} \otimes \mathbf{K}^T \mathbf{K}) \\ &= \mathbf{I}_{sn} + \tau(\mathbf{A} \otimes \mathbf{I}_n)(\mathbf{I}_s \otimes \mathbf{K}^T \mathbf{K}) \\ &= \mathbf{I}_{sn} + \tau(\mathbf{I}_s \otimes \mathbf{K}^T \mathbf{K})\Pi\Pi^{-1}(\mathbf{A} \otimes \mathbf{I}_n) \\ &= \mathbf{I}_{sn} + \tau[(\mathbf{I}_s \otimes \mathbf{K}^T \mathbf{K}) + \tau(\mathbf{I}_s \otimes \mathbf{K}^T \mathbf{K})(\mathbf{A} \otimes \mathbf{I}_n)(\mathbf{I}_s \otimes \mathbf{K}^T \mathbf{K})]\Pi^{-1}(\mathbf{A} \otimes \mathbf{I}_n) \\ &= \mathbf{I}_{sn} + \tau[\mathbf{I}_{sn} + \tau(\mathbf{A} \otimes \mathbf{I}_n)(\mathbf{I}_s \otimes \mathbf{K}^T \mathbf{K})](\mathbf{I}_s \otimes \mathbf{K}^T \mathbf{K})\Pi^{-1}(\mathbf{A} \otimes \mathbf{I}_n) \\ &= \mathbf{I}_{sn} + \tau[\mathbf{I}_{sn} + \tau(\mathbf{A} \otimes \mathbf{K}^T \mathbf{K})](\mathbf{I}_s \otimes \mathbf{K}^T \mathbf{K})\Pi^{-1}(\mathbf{A} \otimes \mathbf{I}_n) \\ &= \mathbf{I}_{sn} + \tau\Pi(\mathbf{I}_s \otimes \mathbf{K}^T \mathbf{K})\Pi^{-1}(\mathbf{A} \otimes \mathbf{I}_n). \end{aligned} \quad (\text{B2})$$

For the uniquely existing inverse $\mathbf{I}_{sn} = \Pi^{-1}\Pi$ holds. Multiplying (B2) with Π^{-1} from the left side therefore yields

$$\mathbf{I}_{sn} = \Pi^{-1} + \tau(\mathbf{I}_s \otimes \mathbf{K}^T \mathbf{K})\Pi^{-1}(\mathbf{A} \otimes \mathbf{I}_n), \quad (\text{B3})$$

which can be re-arranged into (B1).

Appendix C. A-stability

Runge-Kutta methods can either be explicit when \mathbf{A} is a lower-triangular matrix with zero diagonal, or be implicit otherwise. While a single step in an explicit method is usually easier to calculate, it suffers on so-called stiff problems, i.e. differential equations for which the numerical solution proves numerically unstable unless the step size taken is very small. A numerical method that does not suffer from this drawback is called A-stable. The A-stability of a method can be tested by applying it to the test problem $\frac{df}{dx} = kf$, $k \in \mathbb{C}$. A solution derived by a strict A-stable method will decrease (at least

taken absolutely) like the exact solution as $x \rightarrow \infty$ for $\text{Re}(k) < 0$, i.e. the step size is not restricted. Explicit Runge-Kutta methods are not A-stable, while a lot of implicit ones are. In our frame, A-stable implicit Runge-Kutta methods are very effective since the step size is not limited, i.e. the resulting iterative regularization methods need fewer iteration steps. Moreover, this means that the parameter α_k from this point of view is not restricted.